Supplement of Atmos. Chem. Phys., 18, 11471–11491, 2018
https://doi.org/10.5194/acp-18-11471-2018-supplement

Atmospheric Chemistry and Physics
Open Access

Supplement of

Characterization of aerosol composition, aerosol acidity, and organic acid partitioning at an agriculturally intensive rural southeastern US site

Theodora Nah et al.

Correspondence to: Rodney J. Weber (rweber@eas.gatech.edu)

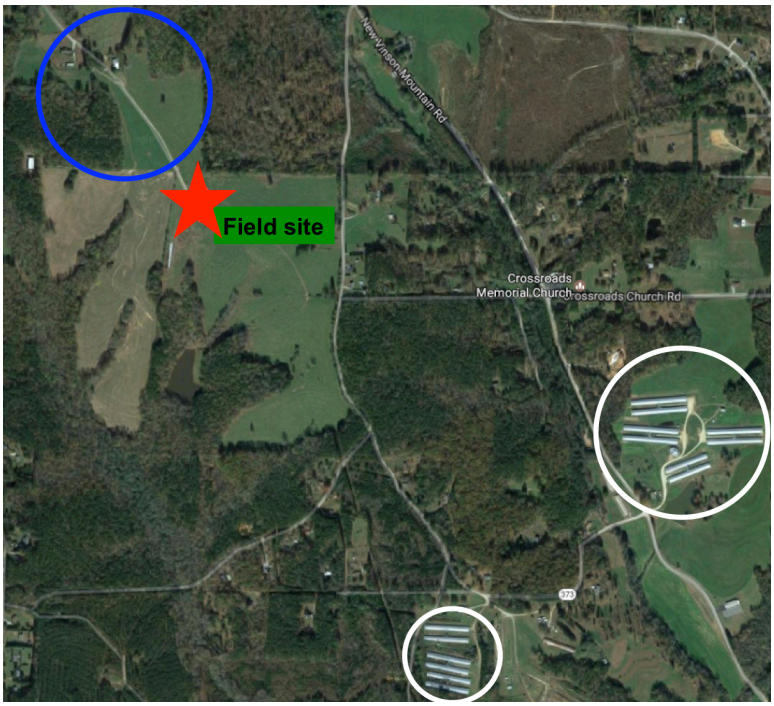

Figure S1: Map of the Yorkville field site (marked by the red diamond) and its surrounding areas (from Google Maps). Locations of nearby cattle-grazing pastures (north-west direction) and poultry CAFOs (south-east direction) are marked by the blue and white circles, respectively.

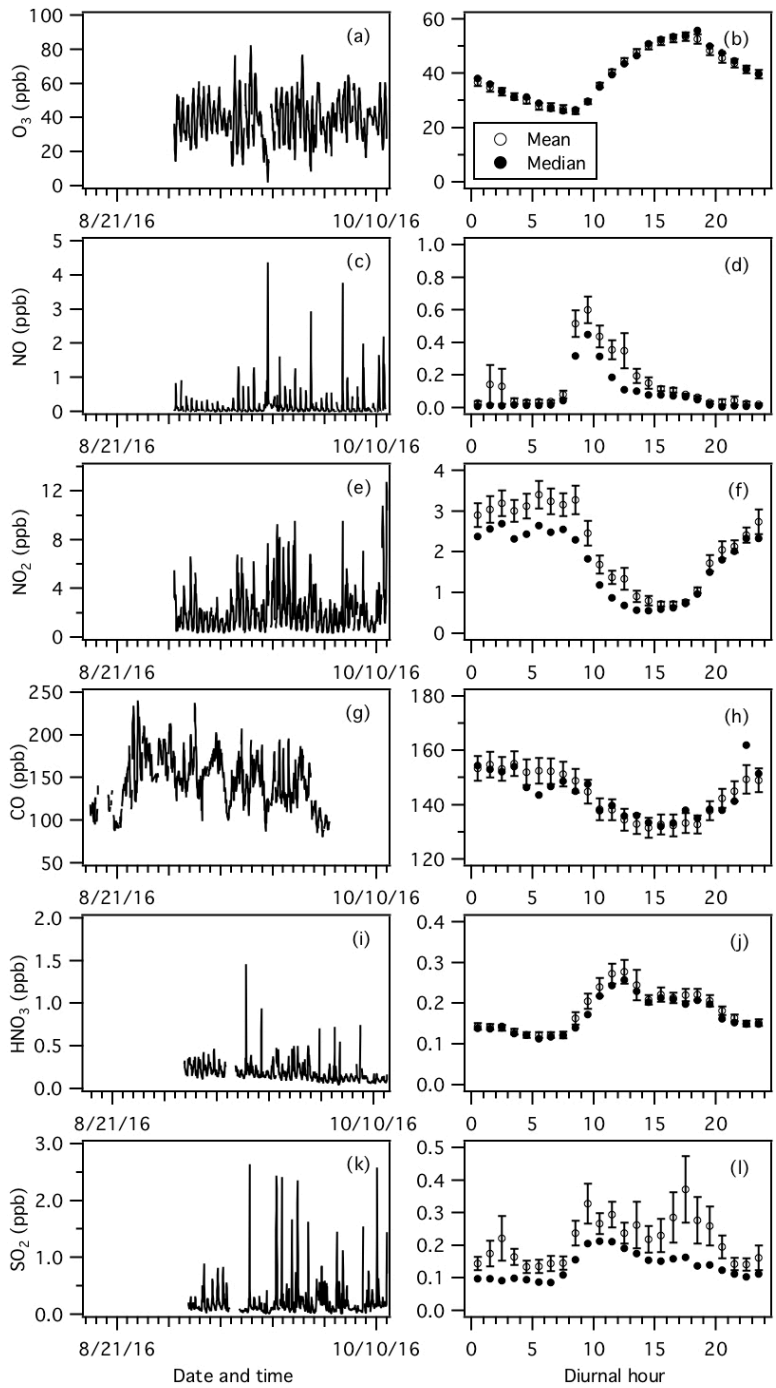

Figure S2: Time series and diurnal profiles of (a and b) O_3, (c and d) NO, (e and f) NO_2, (g and h) CO, (i and j) HNO_3, and (k and l) SO_2. Dates and times displayed are local time. All the concentrations represent averages in 1-hour intervals and the standard errors are plotted as error bars. O_3, NO, NO_2 and CO measurements were provided by the SEARCH network. HNO_3 and SO_2 were measured by the SF_6-CIMS.

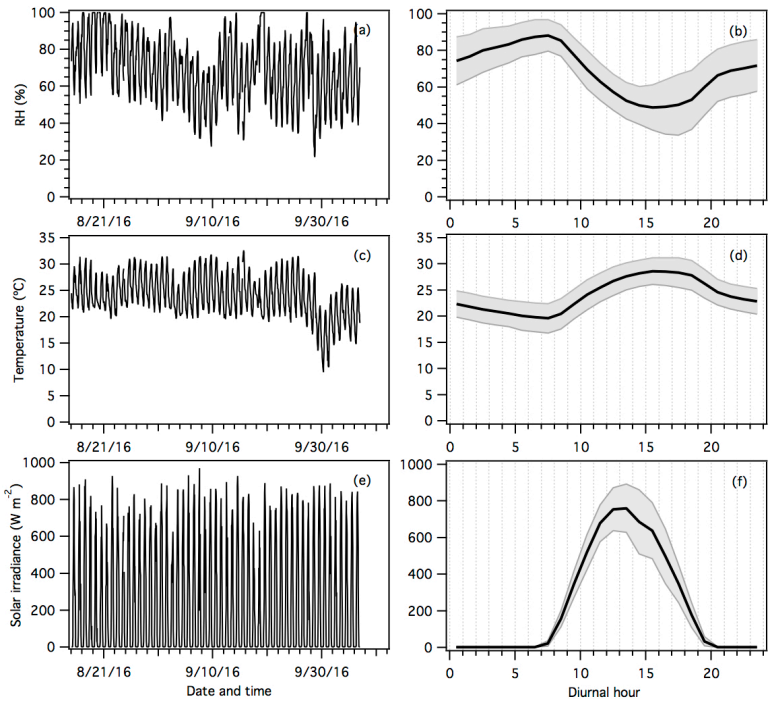

Figure S3: Time series and diurnal profiles of (a and b) RH, (c and d) temperature, and (e and f) solar irradiance. Dates and times displayed are local time. In panels b, d and f, the lines within the shaded area represents the average values. The upper and lower boundaries of the shaded areas mark one standard deviation. RH, temperature and solar irradiance measurements were provided by the SEARCH network.

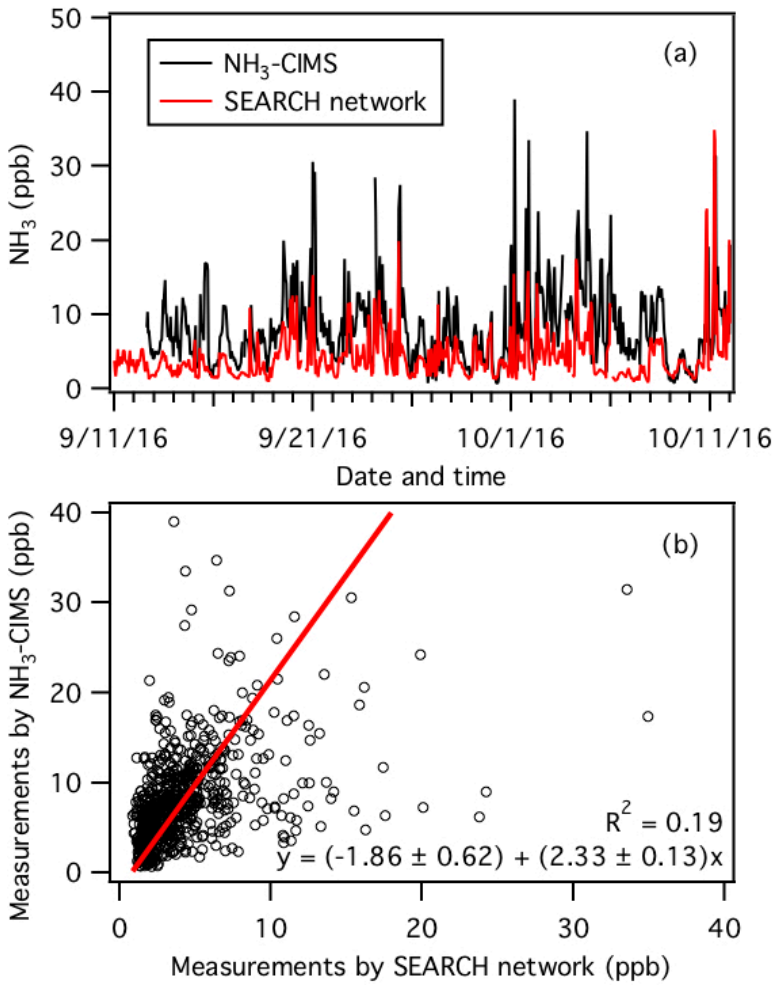

Figure S4: (a) Time series of NH_3 concentrations measured by the NH_3-CIMS and denuder-based instrument operated by the SEARCH network. (b) Comparison of NH_3 concentrations measured by the NH_3-CIMS and denuder-based instrument. The red line is the orthogonal distance regression fit to the data. All the data are displayed as 1-hour averages.

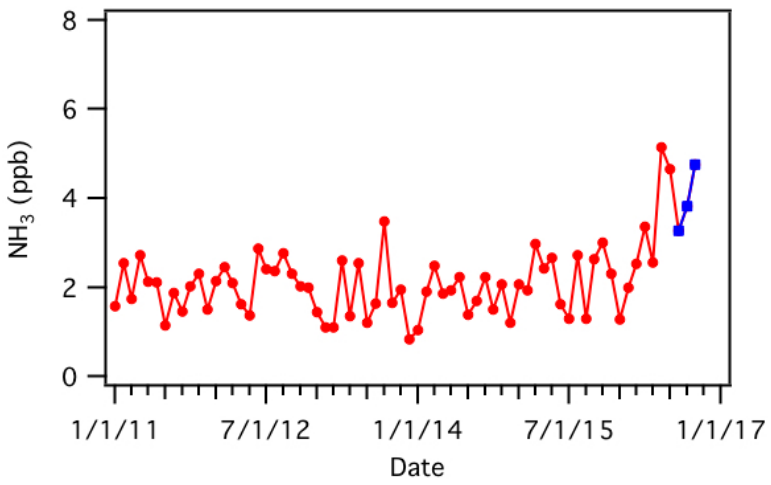

Figure S5: Monthly-averaged NH_3 concentrations at the Yorkville SEARCH monitoring site for 2011 to 2016. These measurements were made using the denuder-based instrument operated by the SEARCH network. Concentrations measured during this study (mid-August to mid-October 2016) are shown in blue.

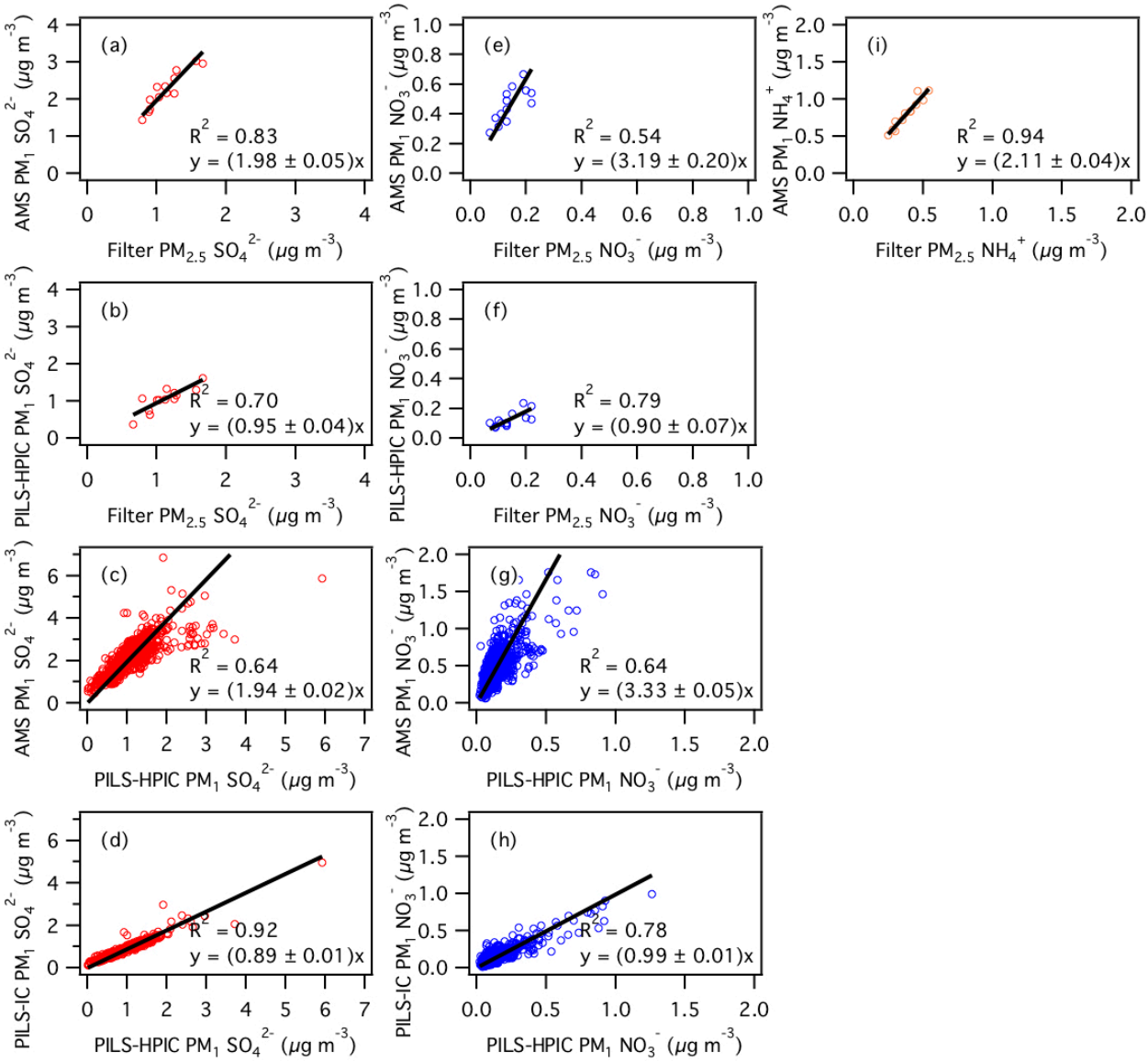

Figure S6: Aerosol (panels a to d) SO_4^{2-}, (panels e to h) NO_3^-, and (i) NH_4^+ comparisons between HR-ToF-AMS, PILS-IC, PILS-HPIC and filters for the entire field study. CDCE values were applied to the raw HR-ToF-AMS data to obtain the mass concentrations shown here (see main text for details). For comparisons between the HR-ToF-AMS, PILS-IC and PILS-HPIC data (panels c, d, g and h), the measurements are averaged over 1 hour intervals. For comparisons with filter data (panels a, b, e, f and i), the HR-ToF-AMS, PILS-IC and PILS-HPIC data are averaged over 24 hour intervals. Orthogonal regression fits are shown. Uncertainties in the fits are 1 standard deviation.

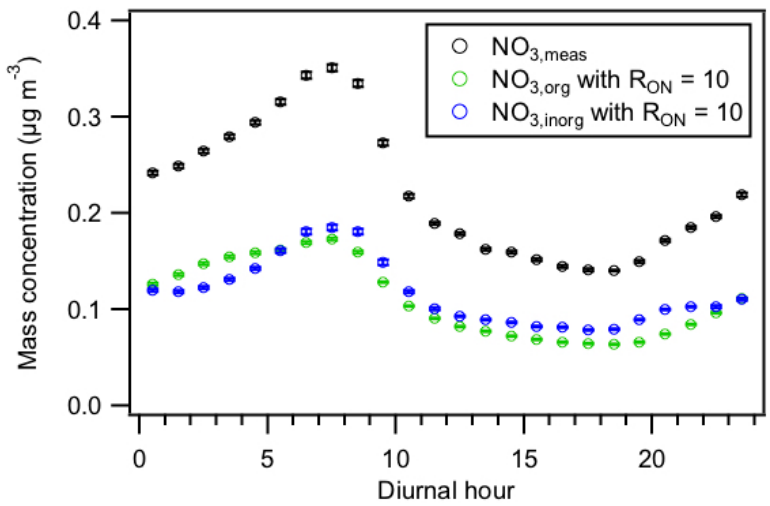

Figure S7: Diurnal profiles of the total nitrate functionality contributed by organic and inorganic nitrates ($NO_{3,meas}$), and the nitrate functionality solely from organic nitrates ($NO_{3,org}$) and inorganic nitrates ($NO_{3,inorg}$). $NO_{3,org}$ and $NO_{3,inorg}$ are estimated using the NO^+/NO_2^+ ratio method as described by Farmer et al. (2010) and Xu et al. (2015). Similar to Xu et al. (2015), we used a R_{ON} (defined here as the NO^+/NO_2^+ ratio for organic nitrates) value of 10 to calculate $NO_{3,org}$ and $NO_{3,inorg}$. All the data shown here represent averages in 1-hour intervals. Error bars shown are the standard errors.

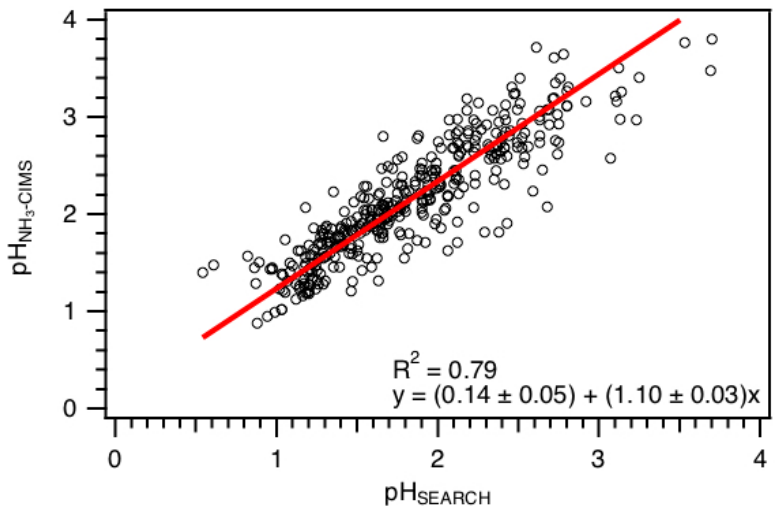

Figure S8: Comparison of predicted PM_1 pH values determined using NH_3-CIMS and SEARCH network's NH_3 measurements as ISORROPIA-II model inputs. The other model inputs are the same. The linear fit is obtained by orthogonal distance regression.

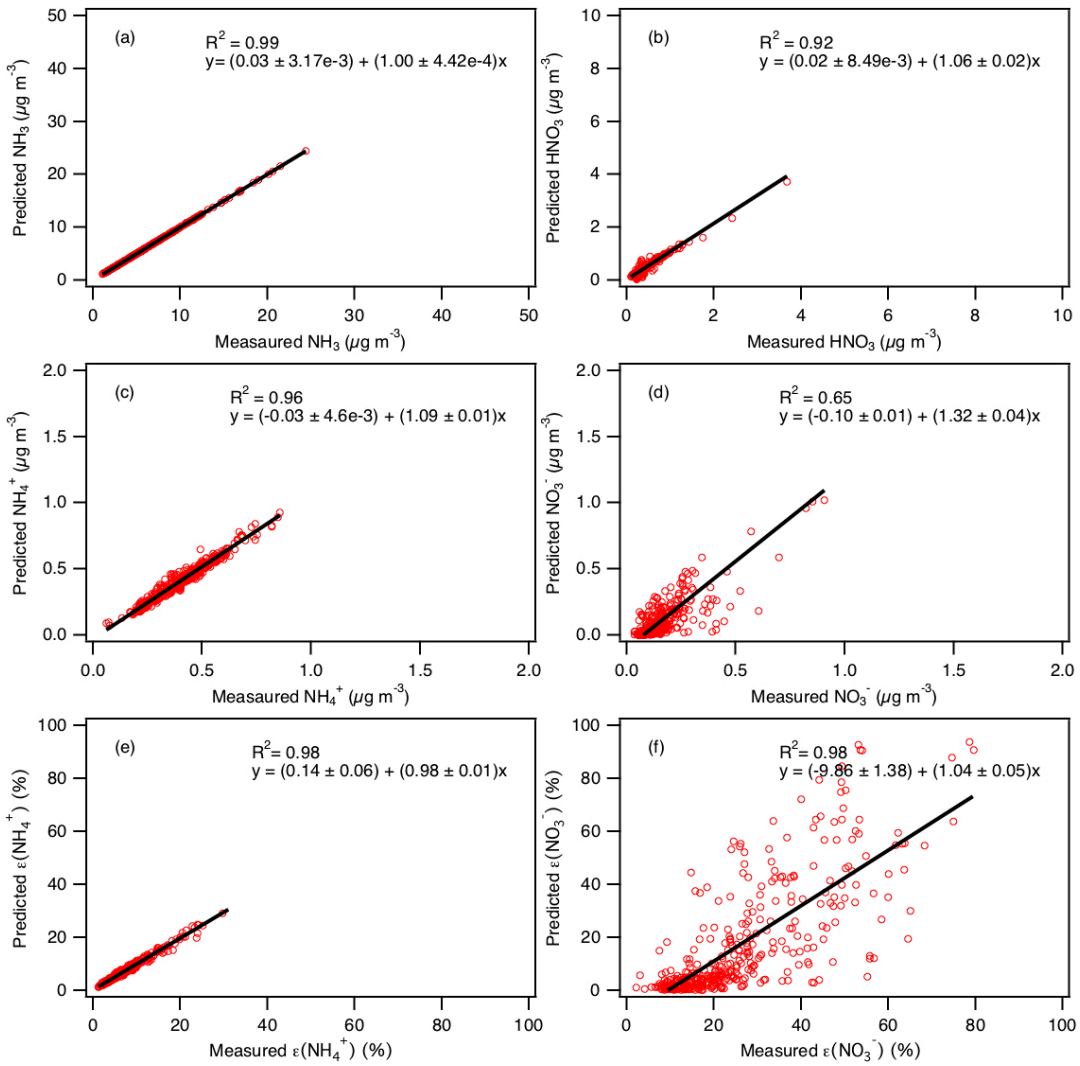

Figure S9: Comparisons of predicted and measured (a) NH_3, (b) HNO_3, (c) NH_4^+, (d) NO_3^-, (e) $\varepsilon(NH_4^+)$, and (f) $\varepsilon(NO_3^-)$. Orthogonal regression fits are shown. Uncertainties in the fits are 1 standard deviation.

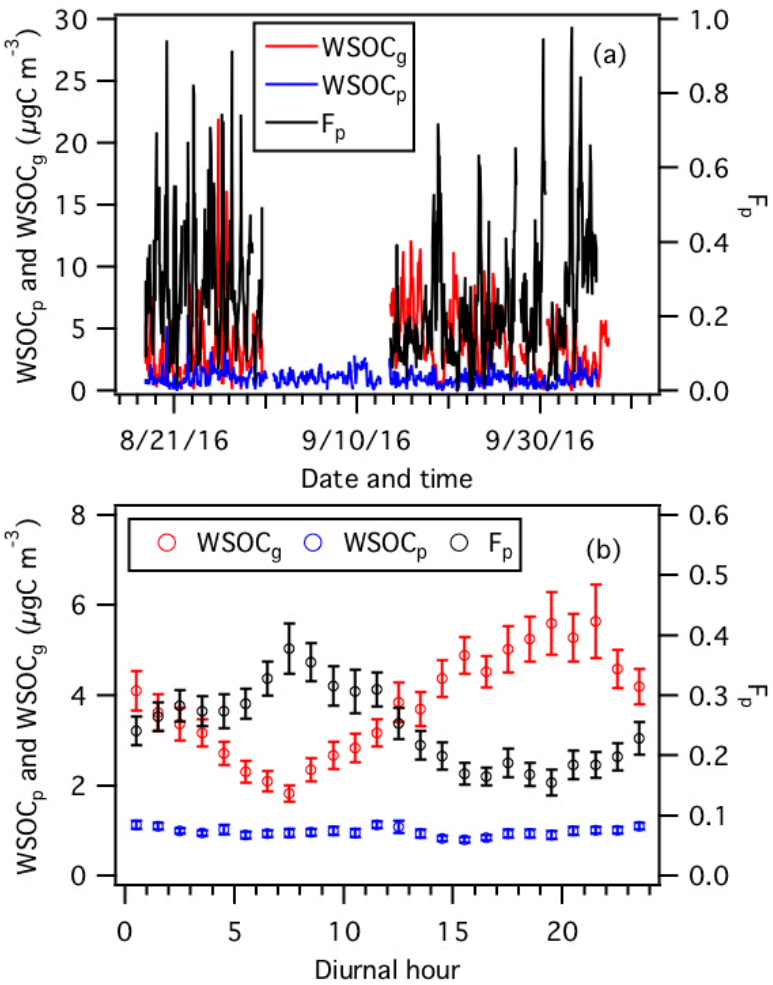

Figure S10: (a) Time series and (b) diurnal profiles of $WSOC_g$, $WSOC_p$ and F_p. Dates and times displayed are local time. All the data shown here represent averages in 1-hour intervals. Error bars shown in panel (b) are the standard errors. $F_p = WSOC_p / (WSOC_p + WSOC_g)$.

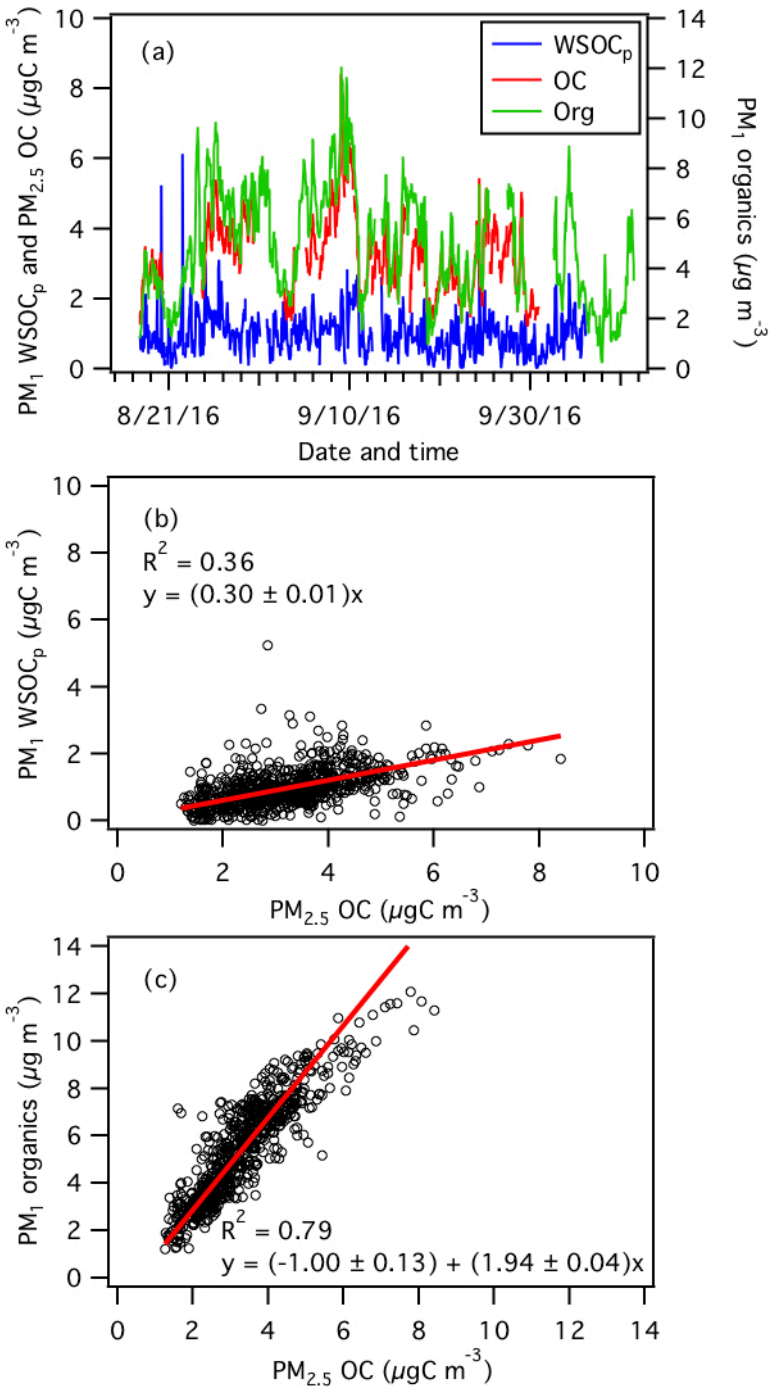

Figure S11: (a) Time series of HR-ToF-AMS organics, $WSOC_p$ and OC. (b) Linear regression correlation between $WSOC_p$ and OC. (c) Linear regression correlation between HR-ToF-AMS organics and OC. All the data shown here represent averages in 1-hour intervals. Note that OC measurements are $PM_{2.5}$, while $WSOC_p$ and HR-ToF-AMS organics measurements are PM_1. Linear fits are obtained by orthogonal distance regression.

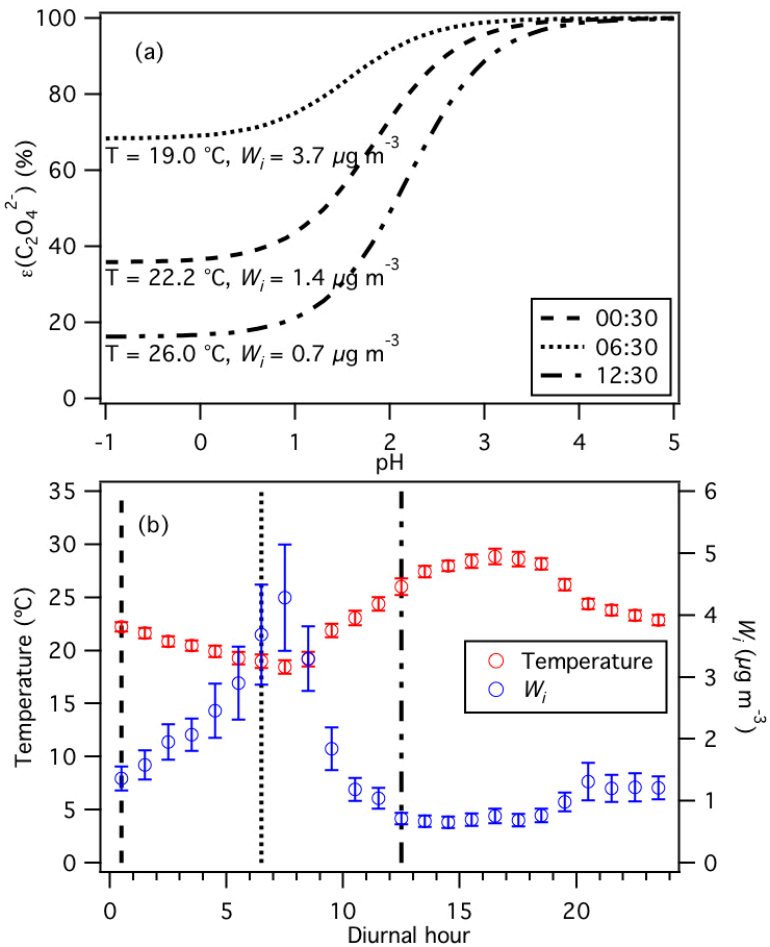

Figure S12: (a) Analytically calculated S curves of $\varepsilon(C_2O_4^{2-})$ at different times of the day: 00:30, 06:30 and 12:30. These S curves are calculated using values obtained from (b) the diurnal profiles of temperature and W_i. The set of 1-hour average temperatures and W_i at diurnal hours 00:30, 06:30 and 12:30 is used to calculate each S curve shown in panel (a). Similar to Fig. 7, we used $\gamma_{C_2H_2O_4}$ = 0.0492 (AIOMFAC predicted) and assumed that $\gamma_{H^+-NO_3^-} = \sqrt{\gamma_{H^+}\gamma_{NO_3^-}} = \sqrt{\gamma_{H^+}\gamma_{C_2HO_4^-}}$ = 0.265 (ISORROPIA-II predicted) to generate these S curves.

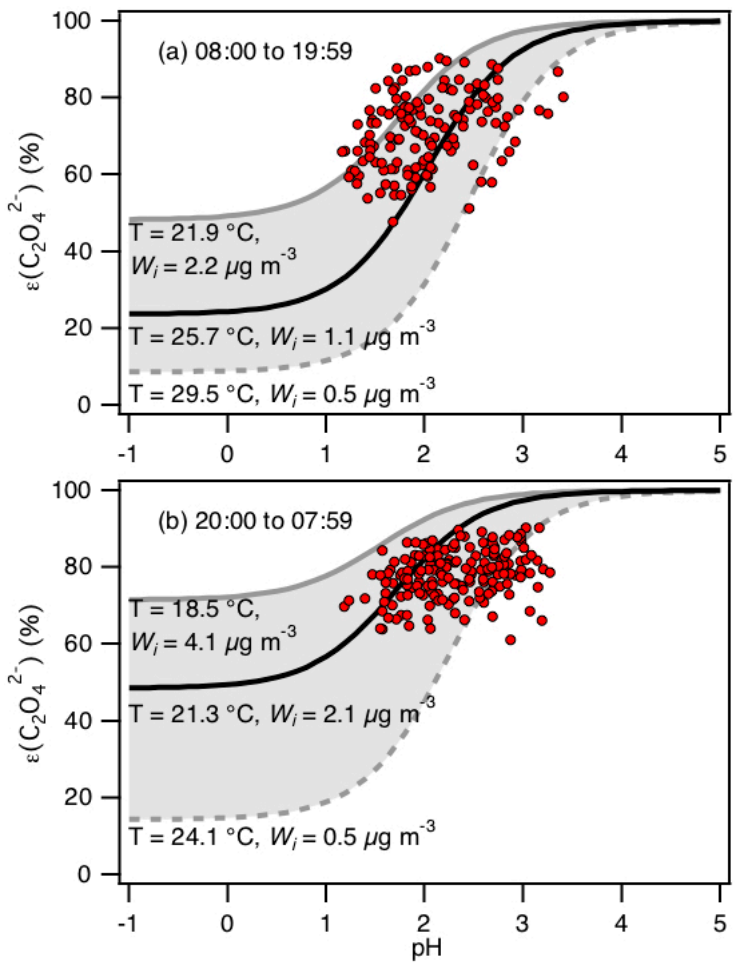

Figure S13: Analytically calculated S curve of ε($C_2O_4^{2-}$) and ambient data from 13 September to 6 October 2016 plotted against ISORROPIA-predicted particle pH. For the ambient data, a narrow range in W_i (0.5 to 4 μg m^{-3}) and RH (20 to 90 %) is chosen to be close to the analytically calculated outputs. We divided the ambient data into two sets: panel (a) 08:00 to 19:59, and panel (b) 20:00 to 07:59. For both analytically calculated S curves, we used $\gamma_{C_2H_2O_4}$ = 0.0492 (AIOMFAC predicted). We also assumed that $\gamma_{H^+}\gamma_{C_2HO_4^-} = \gamma_{H^+}\gamma_{NO_3^-}$, and used the ISORROPIA-predicted $\gamma_{H^+-NO_3^-} = \sqrt{\gamma_{H^+}\gamma_{NO_3^-}}$ = 0.265. In panel (a), we used the average temperature and W_i (25.7 ± 3.8 °C and 1.1 ± 1.1 μg m^{-3}) for the data between 08:00 to 19:59 to calculate the S curve (black line). In panel (b), we used the average temperature and W_i (21.3 ± 2.8 °C and 2.1 ± 2.0 μg m^{-3}) for the data between 20:00 to 07:59 to calculate the S curve (black line). Grey lines in both panels are S curves calculated using one standard deviation from the average temperature and W_i for the two datasets. In panel (a), the dotted grey line is the S curve calculated using 29.5 °C and 0.5 μg m^{-3}

while the solid grey line is the S curve calculated using 21.9 °C and 2.2 μg m^{-3}. In panel (b), the dotted grey line is the S curve calculated using 24.1 °C and 0.5 μg m^{-3} while the solid grey line is the S curve calculated using 18.5 °C and 4.1 μg m^{-3}.

Table S1: List of gas-phase acids measured by SF_6-CIMS, and their measurement uncertainties and detection limits.

Acid	Measurement uncertainty (%)	Detection limits (ppb)[a]
Nitric acid	13	0.20
Formic acid	12	0.03
Acetic acid	12	0.06
Oxalic acid	14	1×10^{-3}
Butyric acid	14	0.03
Glycolic acid	22	2×10^{-3}
Propionic acid	14	6×10^{-3}
Valeric acid	22	0.01
Malonic acid	25	7×10^{-4}
Succinic acid	25	3×10^{-3}

[a]Detection limits are approximated from 3 times the standard deviation values (3σ) of the ion signals measured during background mode. Shown here are the average detection limits of the organic acids for 2.5 min integration periods which corresponds to the length of a background measurement at a 0.04 s duty cycle for each mass.

S1. SF_6-CIMS calibration of gas-phase HNO_3 and organic acids

Detailed descriptions of post-field laboratory calibrations of HNO_3, oxalic, butyric, glycolic, propionic, valeric, malonic and succinic acids can be found in Nah et al. (2018). The response of the CIMS acid signals were measured relative to the sensitivity of $^{34}SO_2$ in these calibration measurements.

The HNO_3 calibration source was a permeation tube (KIN-TEK) whose emission rate was measured using UV optical absorption (Neuman et al., 2003). Solid or liquid samples of oxalic (Sigma Aldrich, ≥ 99 %), butyric (Sigma Aldrich, ≥ 99 %), glycolic (Sigma Aldrich, 99 %), propionic (Sigma Aldrich, ≥ 99.5 %), valeric (Sigma Aldrich, ≥ 99 %), malonic (Sigma Aldrich, ≥ 99.5 %) and succinic (Sigma Aldrich, 99 %) acids were used in calibration measurements. The acid sample was placed in a glass impinger, which was immersed in a water bath at a fixed temperature to provide a constant vapor pressure. For oxalic, butyric, glycolic, propionic and valeric acids, the water bath temperature was set to 0 ˚C. For malonic and succinic acids, the water bath temperature was set to 40 ˚C in order to generate large enough gas phase concentrations for calibration. 6 to 10 mL min^{-1} of nitrogen gas (N_2) was passed over the organic acid in the glass impinger. This organic acid air stream was diluted with different N_2 flows (1 to 5 L min^{-1}) to obtain different mixing ratios of the organic acid. We calculated the mixing ratios based on the acid's emission rate from the impinger or the acid's vapor pressure. Emission rates of gas-phase oxalic, malonic and succinic acids from the impinger were measured by scrubbing the output of the impinger in deionized water, followed by ion chromatography analysis. We measured the vapor pressures of butyric and propionic acids at 0 ˚C using a capacitance manometer (MKS Instruments). We estimated the vapor pressures of glycolic and valeric acids at 0 ˚C using their literature vapor pressures at 25 ˚C and enthalpies of vaporization (Daubert and Danner, 1989; Lide, 1995; Acree and Chickos, 2010).

S2. $WSOC_p$ and OC

We estimated the water-soluble fraction of OC by comparing the $WSOC_p$ and OC measurements. The time series of organics, $WSOC_p$ and OC are shown in Fig. S11a. As shown in Fig. S11b, $WSOC_p$ is moderately correlated with OC at the site. The orthogonal distance regression fit suggests that 30 % of the OC is water-soluble (estimated measurement uncertainty of 19 %),

which is significantly smaller than the fraction (61 %) measured during the SOAS study (Xu et al., 2017). This difference may be due, in part, to the $WSOC_p$/OC ratio for this study being under-estimated. $WSOC_p$ are PM_1 measurements while OC are $PM_{2.5}$ measurements. This is in contrast to the SOAS study where both $WSOC_p$ and OC are $PM_{2.5}$ measurements. PM_1 organics mass concentration is highly correlated with OC and has an orthogonal distance regression slope of 1.94 (Fig. S9c), which is similar to the value (1.92) reported for the SOAS study (Xu et al., 2017).

S3. $C_2H_2O_4$- $C_2O_4^{2-}$ partitioning

Here, we show the detailed derivation of equation (4) in that paper. Equilibrium between gaseous $C_2H_2O_4$ and particle-phase $C_2O_4^{2-}$ involves the dissolution of $C_2H_2O_4$ into the aqueous phase (assuming particles are liquids), followed by dissociation of the dissolved $C_2H_2O_4$:

$$C_2H_2O_4(\mathrm{g}) \leftrightarrow C_2H_2O_4(\mathrm{aq}) \quad H_{C_2H_2O_4}$$

$$C_2H_2O_4(\mathrm{aq}) \leftrightarrow C_2HO_4^-(\mathrm{aq}) + H^+(\mathrm{aq}) \quad K_{a1}$$

$$C_2HO_4^-(\mathrm{aq}) \leftrightarrow C_2O_4^{2-}(\mathrm{aq}) + H^+(\mathrm{aq}) \quad K_{a2}$$

for which the reaction equilibriums are expressed as follows:

$$H_{C_2H_2O_4} = \gamma_{C_2H_2O_4}[C_2H_2O_4]/p_{C_2H_2O_4} \tag{1}$$

$$K_{a1} = \frac{\gamma_{H^+}[H^+]\gamma_{C_2HO_4^-}[C_2HO_4^-]}{\gamma_{C_2H_2O_4}[C_2H_2O_4]} \tag{2}$$

$$K_{a2} = \frac{\gamma_{H^+}[H^+]\gamma_{C_2O_4^{2-}}[C_2O_4^{2-}]}{\gamma_{C_2HO_4^-}[C_2HO_4^-]} \tag{3}$$

where $H_{C_2H_2O_4}$ (mole L^{-1} atm^{-1}) is the Henry's law constant for oxalic acid, K_{a1} and K_{a2} (mole L^{-1}) are the first and second acid dissociation constants for oxalic acid, $p_{C_2H_2O_4}$ (atm) is the partial pressure of oxalic acid in the atmosphere, and γ_i's are activity coefficients. In equations (1) to (3), [x] represents aqueous concentrations (mole L^{-1}).

The total dissolved $C_2H_2O_4$ or particle-phase oxalate ($C_2O_4^{\mathrm{T}}$) can be expressed as:

$$[C_2HO_4^{\mathrm{T}}] = [C_2H_2O_4] + [C_2HO_4^-] + [C_2O_4^{2-}] \tag{4}$$

Using equations (1) to (3), $[C_2O_4^{\mathrm{T}}]$ can be expressed as:

$$[C_2O_4^{\mathrm{T}}] = H_{C_2H_2O_4} p_{C_2H_2O_4} \left(\frac{1}{\gamma_{C_2H_2O_4}} + \frac{K_{a1}}{\gamma_{H^+}\gamma_{C_2HO_4^-}[H^+]} + \frac{K_{a1}K_{a2}}{\gamma_{H^+}\gamma_{H^+}\gamma_{C_2O_4^{2-}}[H^+]^2} \right) \quad (5)$$

The ideal gas law gives:

$$c(C_2H_2O_4) = \frac{p_{C_2H_2O_4}}{RT} \quad (6)$$

where R is the gas constant, T is temperature, and c(x) represents concentration per volume of air (mole m^{-3}). The particle-phase fraction of oxalate can then be expressed as:

$$\varepsilon(C_2O_4^{2-}) = \frac{c(C_2O_4^{\mathrm{T}})}{c(C_2H_2O_4)+c(C_2O_4^{\mathrm{T}})} = \frac{[C_2HO_4^{\mathrm{T}}]W_i}{c(C_2H_2O_4)+[C_2HO_4^{\mathrm{T}}]W_i} \quad (7)$$

where W_i is the particle liquid water content associated with inorganic species (µg m^{-3}; mass per volume of air). Note that the particle liquid water content associated with organic species is not considered in this case, but it can be included. Alternatively, the measured particle water can be used.

By putting equations (5) and (6) into equation (7), $\varepsilon(C_2O_4^{2-})$ can be expressed as:

$$\varepsilon(C_2O_4^{2-}) = \frac{H_{C_2H_2O_4}W_iRT\left(\frac{1}{\gamma_{C_2H_2O_4}}+\frac{K_{a1}}{\gamma_{H^+}\gamma_{C_2HO_4^-}[H^+]}+\frac{K_{a1}K_{a2}}{\gamma_{H^+}\gamma_{H^+}\gamma_{C_2O_4^{2-}}[H^+]^2}\right)}{1+H_{C_2H_2O_4}W_iRT\left(\frac{1}{\gamma_{C_2H_2O_4}}+\frac{K_{a1}}{\gamma_{H^+}\gamma_{C_2HO_4^-}[H^+]}+\frac{K_{a1}K_{a2}}{\gamma_{H^+}\gamma_{H^+}\gamma_{C_2O_4^{2-}}[H^+]^2}\right)} \quad (8)$$

At 298 K, K_{a1} = 5.62 x 10^{-2} mole L^{-1} and K_{a2} = 1.55 x 10^{-4} mole L^{-1} (Haynes, 2014). Assuming that γ_{H^+} = 1, $K_{a1}K_{a2} \ll \gamma_{H^+}\gamma_{H^+}\gamma_{C_2O_4^{2-}}[H^+]^2$ for the conditions of our study. Hence, equation (8) can be simplified to:

$$\varepsilon(C_2O_4^{2-}) \cong \frac{H_{C_2H_2O_4}W_iRT\left(\frac{\gamma_{H^+}\gamma_{C_2HO_4^-}}{\gamma_{C_2H_2O_4}}[H^+]+K_{a1}\right)}{\gamma_{H^+}\gamma_{C_2HO_4^-}[H^+]+H_{C_2H_2O_4}W_iRT\left(\frac{\gamma_{H^+}\gamma_{C_2HO_4^-}}{\gamma_{C_2H_2O_4}}[H^+]+K_{a1}\right)} \quad (9)$$

After accounting for the SI units and substituting $[H^+] = 10^{-pH}$, equation (9) becomes:

$$\varepsilon(C_2O_4^{2-}) \cong \frac{H_{C_2H_2O_4} W_i RT\left(\frac{\gamma_H+\gamma_{C_2HO_4^-}}{\gamma_{C_2H_2O_4}}10^{-pH}+K_{a1}\right)\times 0.987\times 10^{-14}}{\gamma_H+\gamma_{C_2HO_4^-}10^{-pH}+H_{C_2H_2O_4} W_i RT\left(\frac{\gamma_H+\gamma_{C_2HO_4^-}}{\gamma_{C_2H_2O_4}}10^{-pH}+K_{a1}\right)\times 0.987\times 10^{-14}} \quad (10)$$

Note that 0.987 x 10^{-14} comes from using R = 8.314 m^3 Pa K^{-1} mol^{-1}, and hence needing to convert 1 atm to 1 Pa and 1 L to 1 µg. We used the average of $H_{C_2H_2O_4}$ values provided by Clegg et al. (1996), Compernolle and Muller (2014) and Saxena and Hildemann (1996) (6.11 x 10^8 mole L^{-1} atm^{-1} at 25 °C), and accounted for the effect of temperature using equation 19 in Sander (2015). Although K_{a1} also depends on temperature, the K_{a1} value at 25 °C (5.62 x 10^{-2}, (Haynes, 2014)) is used for all the oxalic acid S curve calculations in this paper since equations that determine temperature-dependent K_{a1} values are not available. In addition, the temperatures observed in this study are close to 25 °C.

Figure S12 provides a conceptual picture of how the relationship between $\varepsilon(C_2O_4^{2-})$ and particle pH can change based on the time of the day. Different S curves for $\varepsilon(C_2O_4^{2-})$ are calculated using equation (10) and 1-hour average values obtained from the diurnal profiles of temperature and W_i (specifically at 00:30, 06:30 and 12:30). The S curves are shown to differ substantially due to the diurnal variations of temperature and W_i. For example, a decrease in temperature and an increase in W_i from 00:30 to 06:30 will result in the S curve shifting to the left, which indicates that a substantially higher fraction of gas-phase oxalic acid will partition to the particle phase for a given particle pH at 06:30 compared to at 00:30. Higher W_i also increases the fraction of oxalate that partitions to the particle phase due solely to solubility, as seen from the plateau regions at low pH in Fig. S12. Conversely, an increase in temperature and a decrease in W_i from 06:30 to 12:30 will result in a considerably lower fraction of gas-phase oxalic acid partitioning to the particle phase for a given particle pH at 12:30 compared to at 06:30.

S4. PILS-HPIC denuder efficiency

Post-field laboratory experiments were performed to determine if disagreements between the measured and predicted molar fractions of formic and acetic acid in the particle phase were due to positive biases in particle-phase PILS-HPIC measurements as a result of less than 100 % gas removal denuder efficiency and uptake of gases in the PILS liquid system. While experiments were done solely with formic acid, similar results are expected for acetic acid. In these

experiments, liquid formic acid (Sigma Aldrich, ≥ 99 %) was diluted with ultrapure deionized water and placed in a bubbler. A flow of 18 mL min^{-1} of N_2 was passed through the formic acid in the bubbler. This formic acid air stream was then passed through a nafion dryer and diluted with 52 L min^{-1} of N_2. Two experiments were performed. In the first experiment, the diluted formic acid air flow was introduced directly into the PILS, which was connected to a Metrohm 761 Compact IC (Metrohm AG). In the second experiment, the diluted formic acid air flow was passed through a 28 cm parallel plate carbon denuder (Sunset Lab) prior to introduction into the PILS-IC system.

Our experiments showed that the IC detected formate when the diluted formic acid air flow was introduced directly into the PILS-IC system. IC analysis revealed that the gas-phase formic acid concentration was ~75 μg m^{-3}. However, no formate was detected above the limit of detection (0.02 μg m^{-3}) when the diluted formic acid air flow was passed through the carbon denuder prior to introduction into the PILS-IC system. These measurements indicated that the carbon denuder has a ≥ 99.97 % formic acid gas removal efficiency. Hence, these experiments indicate that the carbon denuder removes the formic acid gas completely. We conclude that disagreements between the measured and predicted molar fractions of formic and acetic acid in the particle phase were not due to positive biases in particle-phase formate and acetate PILS-HPIC measurements as a result of less than 100 % gas removal denuder efficiency.

S5. Particle-phase formic and acetic acid dimers

Previous studies have shown that formic and acetic acid dimers may form in the aqueous phase (Schrier et al., 1964; Gilson et al., 1997; Chen et al., 2008). If the aforementioned acid dimers are present in aerosols, equilibrium between gas-phase formic/acetic acid (denoted as HA) and particle-phase formate/acetate (denoted as A^-) will differ from that predicted assuming no dimers existed, as done in the main text.

The dissolution of HA into the aqueous phase (assuming particles are liquids), followed by the formation of particle-phase dimers (denoted as $((HA)_2)$ and dissociation of the dissolved HA:

$$HA\ (\mathrm{g}) \leftrightarrow HA\ (\mathrm{aq}) \quad H_{HA}$$

$$HA\ (\mathrm{aq}) \leftrightarrow (HA)_2\ (\mathrm{aq}) \quad K_{dim}$$

$$HA\ (\mathrm{aq}) \leftrightarrow A^{-}\ (\mathrm{aq}) + H^{+}(\mathrm{aq}) \quad K_{a1}$$

for which the reaction equilibriums are expressed as follows:

$$H_{HA} = \gamma_{HA}[HA]/p_{HA} \tag{11}$$

$$K_{dim} = \frac{[(HA)_2]}{[HA]^2} \tag{12}$$

$$K_{a1} = \frac{\gamma_{A^-}[A^-]\gamma_{H^+}[H^+]}{\gamma_{HA}[HA]} \tag{13}$$

where H_{HA} (mole L^{-1} atm^{-1}) is the Henry's law constant for formic or acetic acid, K_{a1} (mole L^{-1}) is the first acid dissociation constants for formic or acetic acid, p_{HA} (atm) is the partial pressure of formic or acetic acid in the atmosphere, K_{dim} (L mole^{-1}) is the dimerization constant, and γ_i's are activity coefficients. In equations (11) to (13), [x] represents aqueous concentrations (mole L^{-1}).

The total dissolved formate or acetate (A^{T}) can be expressed as:

$$[A^T] = [HA] + [A^-] + [(HA)_2] \tag{14}$$

Using equations (11) to (13), $[A^T]$ can be expressed as:

$$[A^T] = H_{HA}p_{HA}\left(\frac{1}{\gamma_{HA}} + \frac{K_{a1}}{\gamma_{H^+}\gamma_{A^-}[H^+]} + \frac{K_{dim}H_{HA}p_{HA}}{\gamma_{HA}\gamma_{HA}}\right) \tag{15}$$

The ideal gas law gives:

$$c(HA) = \frac{p_{HA}}{RT} \tag{16}$$

where R is the gas constant, T is temperature, and c(x) represents concentration per volume of air (mole m^{-3}). The particle-phase fraction of formate or acetate can then be expressed as:

$$\varepsilon(A^-) = \frac{c(A^T)}{c(HA)+c(A^T)} = \frac{[A^T]W_i}{c(HA)+[A^T]W_i} \tag{17}$$

where W_i is the particle liquid water content associated with inorganic species (μg m^{-3}; mass per volume of air). Particle liquid water content associated with organic species is not considered in this case, but it can be included. Alternatively, the measured particle water can be used.

By putting equations (15) and (16) into equation (17), and accounting for the SI units, $\varepsilon(A^-)$ can ultimately be expressed as:

$$\varepsilon(A^-) = \frac{H_{H_{HA}} W_i RT\left(\frac{1}{\gamma_{HA}} + \frac{K_{a1}}{\gamma_{H^+}\gamma_{A^-}10^{-pH}} + \frac{K_{dim} H_{HA} p_{HA}}{\gamma_{HA}\gamma_{HA}}\right) \times 0.987 \times 10^{-14}}{1 + H_{H_{HA}} W_i RT\left(\frac{1}{\gamma_{HA}} + \frac{K_{a1}}{\gamma_{H^+}\gamma_{A^-}10^{-pH}} + \frac{K_{dim} H_{HA} p_{HA}}{\gamma_{HA}\gamma_{HA}}\right) \times 0.987 \times 10^{-14}} \quad (18)$$

At 298 K, K_{a1} values are 1.78 x 10^{-4} mole L^{-1} and 1.75 x 10^{-5} mole L^{-1} for formic and acetic acid, respectively (Haynes, 2014). K_{dim} values are 0.56 L $mole^{-1}$ and 0.92 L $mole^{-1}$ for formic and acetic acid, respectively (Chen et al., 2008). Temperature-dependent H_{HA} values for formic and acetic acid can be obtained from Sander (2015). p_{HA} can be calculated from the measured gas-phase formic or acetic acid concentrations (μg m^{-3}) and the ideal gas law. We used the web version of AIOMFAC (www.aiomfac.caltech.edu) (Zuend et al., 2008; Zuend et al., 2011; Zuend et al., 2012) to compute study-averaged γ_{HA} values of 0.334 and 2.150 for formic and acetic acid, respectively. We assumed that $\gamma_{H^+}\gamma_{A^-} = \gamma_{H^+}\gamma_{NO_3^-}$ = 0.07 for both formic and acetic acid.

Comparison of S curves generated from equation (18) and those generated from equations (5) and (6) in the main text (which assumed that no dimers existed) showed that accounting for the presence of acid dimers increased predicted $\varepsilon(A^-)$ values by less than 1 % for particle pH 0.9 to 3.8 (i.e., pH values in this study). S curves generated by equation (18) also do not match our measured molar fractions of formic and acetic acid in the particle phase. This analysis shows that the molar fractions of formic and acetic acid in the particle phase do not change substantially when the presence of particle-phase acid dimers is accounted for due to the somewhat low H_{HA} values for formic and acetic acid. Hence, disagreements between the measured and predicted molar fractions of formic and acetic acid in the particle phase are not due to the presence of particle-phase formic and acetic acid dimers.

References

Acree, W., and Chickos, J. S.: Phase Transition Enthalpy Measurements of Organic and Organometallic Compounds. Sublimation, Vaporization and Fusion Enthalpies From 1880 to 2010, J. Phys. Chem. Ref. Data, 39, 942, 10.1063/1.3309507, 2010.

Chen, J. H., Brooks, C. L., and Scheraga, H. A.: Revisiting the carboxylic acid dimers in aqueous solution: Interplay of hydrogen bonding, hydrophobic interactions, and entropy, Journal of Physical Chemistry B, 112, 242-249, 10.1021/jp074355h, 2008.

Clegg, S. L., Brimblecombe, P., and Khan, L.: The Henry's law constant of oxalic acid and its partitioning into the atmospheric aerosol, Idojaras, 100, 51-68, 1996.

Compernolle, S., and Muller, J. F.: Henry's law constants of diacids and hydroxy polyacids: recommended values, Atmos. Chem. Phys., 14, 2699-2712, 10.5194/acp-14-2699-2014, 2014.

Daubert, T. E., and Danner, R. P.: Physical and thermodynamic properties of pure chemicals: data compilation, Taylor & Francis, Washington, DC, 1989.

Farmer, D. K., Matsunaga, A., Docherty, K. S., Surratt, J. D., Seinfeld, J. H., Ziemann, P. J., and Jimenez, J. L.: Response of an aerosol mass spectrometer to organonitrates and organosulfates and implications for atmospheric chemistry, Proceedings of the National Academy of Sciences of the United States of America, 107, 6670-6675, 10.1073/pnas.0912340107, 2010.

Gilson, M. K., Given, J. A., Bush, B. L., and McCammon, J. A.: The statistical-thermodynamic basis for computation of binding affinities: A critical review, Biophysical Journal, 72, 1047-1069, 10.1016/s0006-3495(97)78756-3, 1997.

Haynes, W. M.: CRC handbook of chemistry and physics: A ready-reference book of chemical and physical data. , Boca Raton: CRC Press, 2014.

Lide, D. R.: CRC handbook of chemistry and physics: a ready-reference book of chemical and physical data, CRC Press, Boca Raton, FL, 1995.

Nah, T., Ji, Y., Tanner, D. J., Guo, H., Sullivan, A. P., Ng, N. L., Weber, R. J., and Huey, L. G.: Real-time measurements of gas-phase organic acids using SF6- chemical ionization mass spectrometry, Atmos. Meas. Tech. Discuss., 2018, 1-40, 10.5194/amt-2018-46, 2018.

Neuman, J. A., Ryerson, T. B., Huey, L. G., Jakoubek, R., Nowak, J. B., Simons, C., and Fehsenfeld, F. C.: Calibration and evaluation of nitric acid and ammonia permeation tubes by UV optical absorption, Environmental Science & Technology, 37, 2975-2981, 10.1021/es0264221, 2003.

Sander, R.: Compilation of Henry's law constants (version 4.0) for water as solvent, Atmos. Chem. Phys., 15, 4399-4981, 10.5194/acp-15-4399-2015, 2015.

Saxena, P., and Hildemann, L. M.: Water-soluble organics in atmospheric particles: A critical review of the literature and application of thermodynamics to identify candidate compounds, Journal of Atmospheric Chemistry, 24, 57-109, 10.1007/bf00053823, 1996.

Schrier, E. E., Pottle, M., and Scheraga, H. A.: The Influence of Hydrogen and Hydrophobic Bonds on the Stability of the Carboxylic Acid Dimers in Aqueous Solution, Journal of the American Chemical Society, 86, 3444-3449, 10.1021/ja01071a009, 1964.

Xu, L., Suresh, S., Guo, H., Weber, R. J., and Ng, N. L.: Aerosol characterization over the southeastern United States using high-resolution aerosol mass spectrometry: spatial and seasonal variation of aerosol composition and sources with a focus on organic nitrates, Atmos. Chem. Phys., 15, 7307-7336, 10.5194/acp-15-7307-2015, 2015.

Xu, L., Guo, H. Y., Weber, R. J., and Ng, N. L.: Chemical Characterization of Water-Soluble Organic Aerosol in Contrasting Rural and Urban Environments in the Southeastern United States, Environmental Science & Technology, 51, 78-88, 10.1021/acs.est.6b05002, 2017.

Zuend, A., Marcolli, C., Luo, B. P., and Peter, T.: A thermodynamic model of mixed organic-inorganic aerosols to predict activity coefficients, Atmos. Chem. Phys., 8, 4559-4593, 10.5194/acp-8-4559-2008, 2008.

Zuend, A., Marcolli, C., Booth, A. M., Lienhard, D. M., Soonsin, V., Krieger, U. K., Topping, D. O., McFiggans, G., Peter, T., and Seinfeld, J. H.: New and extended parameterization of the

thermodynamic model AIOMFAC: calculation of activity coefficients for organic-inorganic mixtures containing carboxyl, hydroxyl, carbonyl, ether, ester, alkenyl, alkyl, and aromatic functional groups, Atmos. Chem. Phys., 11, 9155-9206, 10.5194/acp-11-9155-2011, 2011.

Zuend, A., Marcolli, C., Luo, B. P., and Peter, T.: A thermodynamic model of mixed organic-inorganic aerosols to predict activity coefficients (vol 8, pg 4559, 2008), Atmos. Chem. Phys., 12, 10075-10075, 10.5194/acp-12-10075-2012, 2012.